Journal of Computational and Applied Mathematics 235 (2011) 3760–3767

Contents lists available at ScienceDirect

Journal of Computational and Applied Mathematics

journal homepage: www.elsevier.com/locate/cam

Large eddy simulation of coherent structures in rectangular methane non-premixed flame

Y.C. Guo [a,*], P. Jiang [a], C.K. Chan [b], W.Y. Lin [a]

[a] Department of Engineering Mechanics, Tsinghua University, Beijing 100084, China

[b] Department of Applied Mathematics, The Hong Kong Polytechnic University, Hung Hom, Kowloon, Hong Kong

ARTICLE INFO

Keywords:
Rectangular jets
Large eddy simulation
Coherent structure
Non-premixed flame

ABSTRACT

Large eddy simulation of a three-dimensional spatially developing transitional free methane non-premixed flame is performed. The solver of the governing equations is based upon a projection method. The Smagorinsky model is utilized for the turbulent subgrid scale terms. A global reaction mechanism is applied for the simulation of methane/air combustion. Simulation results clearly illustrate the coherent structure of the rectangular non-premixed flame, consisting of three distinct zones in the near field. Periodic characteristics of the coherent structures in the rectangular non-premixed flame are discussed. The predicted structure of the flame is in good agreement with the experimental results. Distributions of species concentrations across the flame surfaces are illustrated and typical flame structures in the far field are analyzed. Local mass fraction analysis and flow visualization indicate that the black spots of the flames are due to strong entrainment of oxygen into the central jet by streamwise vortices, and breaking up of the flame is caused by an enormous amount of entrainment of streamwise vortices as well as stretching of spanwise vortices at the bottom of the flame.

© 2011 Elsevier B.V. All rights reserved.

1. Introduction

Since the pioneering work on coherent structures in turbulent flow by Crow and Champagne [1], a lot of research has been carried out concerning the mechanism and role of coherent structures in various types of flow such as near-wall boundaries, jet flows and wakes. It is generally recognized that development of coherent structures affects the flow in terms of entrainment, mixing, noise generation etc.

A lot of experimental and numerical results on rectangular jets have been reported. Sfeir's work [2] on rectangular jets was concerned with the effect of inlet geometry on the evolution of jets. Krothapalli et al. [3] obtained detailed measurements of mean velocities and shear stresses in both the major and minor planes, with aspect ratios (AR) between 5.5 and 16.7. With studies of turbulence decay along the centerline, it was found that the jet could be characterized by the presence of three distinct regions, namely a potential core region, a two-dimensional region and an axisymmetric region. More recently, Miller et al. [4] carried out a comprehensive numerical study and illustrated the detailed axis-switching phenomenon and entrainment rate of various non-circular jets including elliptic, rectangular and triangular jets. Grinstein and Kalilasanath [5] extended the numerical work to reactive square jets, so as to consider the effects of chemical exothermicity and density differences, particularly in terms of the entrainment rate. The comprehensive development of local vortex structure of square

* Corresponding author.
E-mail address: guoyc@mail.tsinghua.edu.cn (Y.C. Guo).

0377-0427/$ – see front matter © 2011 Elsevier B.V. All rights reserved.
doi:10.1016/j.cam.2011.01.022

Nomenclature

C_s	turbulence SGS model coefficient
L_1, L_2	nozzle dimensions
p	pressure
S_{ij}	strain rate tensor
t	non-dimensional time
T	temperature
U_0	nozzle exit velocity in the x direction (streamwise velocity)
U_{con}	convective velocity at the outlet
u_i	$i = 1, 2, 3$; ith velocity component
u_m	local centerline streamwise mean velocity
$\overrightarrow{V^*}$	intermediate velocity vector
x, y, z	non-dimensional streamwise, transverse and spanwise coordinates
$y_{1/2}$, $z_{1/2}$	half-velocity widths
Y	species mass fraction

Greek symbols

μ	molecular viscosity of air
μ_t	subgrid viscosity
τ_{ij}	subgrid scale Reynolds stress
Δ	filtering box size
Δx, Δy, Δz	grid size in the x, y, and z directions
ω_{CH_4}	reaction rate of methane

jets, using large eddy simulation, was presented in [6]. Rembold et al. [7] investigated the transitional stage of a rectangular jet with $AR = 5$ by means of direct numerical simulation (DNS). Distributions of velocities together with transverse and spanwise Reynolds stresses were given.

Despite the above experimental and numerical work, more work is needed to explain the instantaneous vortical development of rectangular jets. In addition, most of these investigations of rectangular jets were on isothermal flows. Vortex–flame interactions are important in a turbulent flame and have received substantial attention in recent years [8,9]. These observations suggested a significant difference in the coherent structures for isothermal and reacting jets. It is therefore necessary to investigate the effect of instantaneous vortical development on the flame structure in a rectangular non-premixed flame.

In this paper, an isothermal jet and a methane non-premixed flame jet from rectangular nozzles are numerically simulated. The focus is on the coherent structure development of the rectangular jets by means of large eddy simulation. The focus is on the periodic characteristics of coherent structures in the near field as well as flame structures in the far field of the methane non-premixed flame.

2. The formulation and numerical procedure

2.1. The configuration of the simulation

In this paper, the isothermal jet and methane non-premixed jet from a rectangular nozzle are numerically simulated with LES. A schematic diagram of the jet configuration is shown in Fig. 1. The central plane determined by lines AO and OC is referred to as the major plane, and that determined by lines BO and OC is the minor plane. In addition, the z-axis and y-axis in Fig. 1 are the major and minor axes respectively. In this paper, the computational domain is taken as $60L_2 \times 10.83L_2 \times 10.83L_2$, where L_2 is the shorter side of the rectangle.

2.2. Governing equations

In recent years, LES has become an effective method for studying turbulent combustion processes [10,11]. With the box-filter applied to LES, the filtered non-dimensionalized governing equations are given as follows:

continuity equation:

$$\frac{\partial \bar{\rho}}{\partial t} + \frac{\partial \bar{\rho}\tilde{u}_j}{\partial x_j} = 0, \tag{1}$$

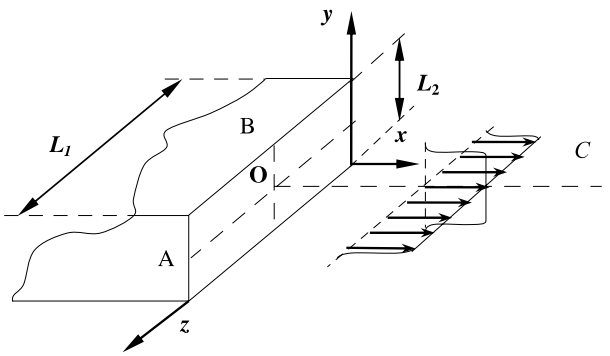

Fig. 1. Schematic diagram of the rectangular jet.

momentum equation:

$$\frac{\partial \bar{\rho}\tilde{u}_i}{\partial t} + \frac{\partial \bar{\rho}\tilde{u}_i\tilde{u}_j}{\partial x_j} = -\frac{\partial \bar{p}}{\partial x_i} + \frac{\partial}{\partial x_j}\left[\mu\left(\frac{\partial \tilde{u}_i}{\partial x_j} + \frac{\partial \tilde{u}_j}{\partial x_i} - \frac{2}{3}\frac{\partial \tilde{u}_k}{\partial x_k}\delta_{ij}\right)\right] - \frac{\partial \tau_{ij}}{\partial x_j} + (1-\bar{\rho})g_i\delta_{1i}, \tag{2}$$

species equation:

$$\frac{\partial \bar{\rho}\tilde{Y}_s}{\partial t} + \frac{\partial \bar{\rho}\tilde{Y}_s\tilde{u}_j}{\partial x_j} = \frac{\partial}{\partial x_j}\left(\frac{\mu}{S_C}\frac{\partial \tilde{Y}_s}{\partial x_j}\right) - \frac{\partial \gamma_j}{\partial x_j} + \bar{\omega}_s, \tag{3}$$

energy equation:

$$\frac{\partial \bar{\rho}\tilde{c}_p\tilde{T}}{\partial t} + \frac{\partial \bar{\rho}\tilde{c}_p\tilde{T}\tilde{u}_j}{\partial x_j} = \frac{\partial}{\partial x_j}\left(\frac{\mu\tilde{c}_p}{Pr}\frac{\partial \tilde{T}}{\partial x_j}\right) - \frac{\partial \theta_j}{\partial x_j} + \tilde{\omega}_{CH_4}Q_{CH_4}, \tag{4}$$

ideal gas equation:

$$\bar{p}_0 = \bar{\rho}R\tilde{T}\sum\frac{\tilde{Y}_s}{M_s}, \tag{5}$$

where $\tau_{ij} = \bar{\rho}\overline{u_iu_j} - \bar{\rho}\tilde{u}_i\tilde{u}_j$, $\gamma_j = \bar{\rho}\overline{Y_su_j} - \bar{\rho}\tilde{Y}_s\tilde{u}_j$ and $\theta_j = \bar{\rho}\overline{c_pTu_j} - \bar{\rho}\tilde{c}_p\tilde{T}\tilde{u}_j$ are the subgrid Reynolds stresses, subgrid turbulent mass fluxes and subgrid turbulent heat fluxes respectively, with the sign "$\bar{\ }$" denoting spatial filtering for density and "$\tilde{\ }$" denoting Favre filtering.

2.3. Turbulent SGS models

The subgrid Reynolds stresses can be modeled using the Smagorinsky model [12] and the simplified Boussinesq approximation, as follows:

$$\tau_{ij} = -2\bar{\rho}(C_s\Delta)^2\left|\tilde{\mathbf{S}}\right|\left(\tilde{S}_{ij} - \frac{1}{3}\tilde{S}_{kk}\delta_{ij}\right) \equiv -2\mu_T\left(\tilde{S}_{ij} - \frac{1}{3}\tilde{S}_{kk}\delta_{ij}\right), \tag{6}$$

where $\left|\tilde{S}\right| = (2\tilde{S}_{ij}\tilde{S}_{ij})^{1/2}$, $\tilde{S}_{ij} = \frac{1}{2}(\frac{\partial \tilde{u}_i}{\partial x_j} + \frac{\partial \tilde{u}_j}{\partial x_i})$, and $\mu_T = \bar{\rho}(C_s\Delta)^2\left|\tilde{\mathbf{S}}\right|$. C_s is the subgrid scale model coefficient with a value of 0.025 chosen for this paper to allow comparison with the dynamic SGS model for simulating isothermal flow in our previous study [13]. The grid filter width is determined by $\Delta = (\Delta x\Delta y\,\Delta z)^{\frac{1}{3}}$, where Δx, Δy and Δz are grid sizes for different coordinate directions.

Similarly, the subgrid turbulent mass fluxes and subgrid turbulent heat fluxes can be modeled as

$$\gamma_j = \frac{\mu_T}{S_C}\frac{\partial \tilde{Y}_s}{\partial x_j} \quad \text{and} \quad \theta_j = \frac{\mu_T\tilde{c}_p}{Pr}\left(\frac{\partial \tilde{T}}{\partial x_j}\right). \tag{7}$$

2.4. Solution of the governing equations

A projection method [14], which treats pressure as an intermediate variable satisfying the continuity equation, is utilized in solving the governing equations. Equations for Y_s and T are initially solved explicitly from the values of the previous time step. Density is then calculated from the ideal gas equation. The momentum equations without the pressure term are solved to obtain the predicted velocity field $\vec{\tilde{V}}^*$. With this predicted velocity field, the Poisson equation for pressure is solved, using

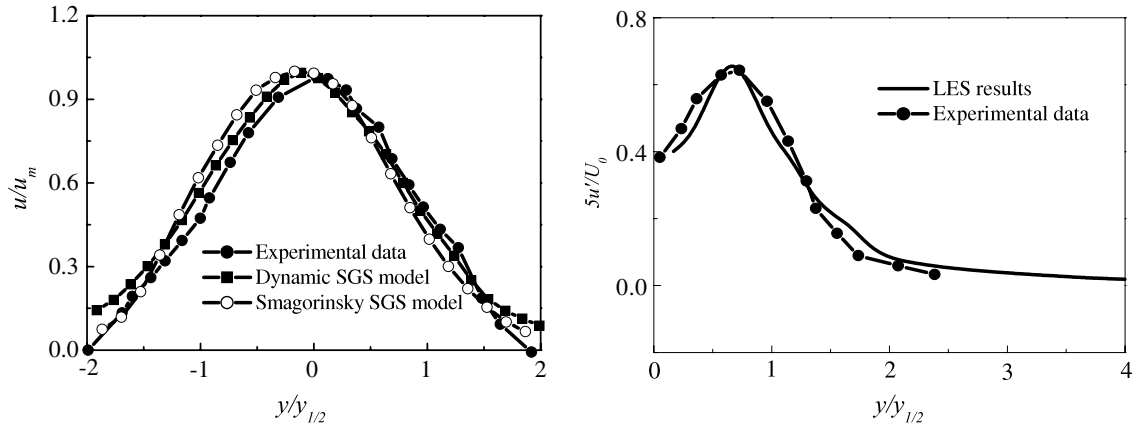

(a) Streamwise velocity.

(b) Turbulent fluctuation velocity.

Fig. 2. Velocity distribution of the isothermal flow at $x = 7$.

a direct solver based on the Fourier cyclic odd–even reduction algorithm. With the pressure Poisson equation solved, the predicted velocity is finally corrected.

All variables are discretized on a three-dimensional staggered Cartesian grid with uniform cell size. Velocity components are located at the cell faces, and scalar variables, such as pressure and temperature, are located at cell centers. The standard Eulerian explicit scheme is used for the temporal integration of velocities. A three-point second-order upwind scheme is used for the discretization of the convection term and a five-point fourth-order central difference scheme is used for the diffusion term.

3. Results and discussion

3.1. The isothermal jet

In order to compare with experimental data, the nozzle dimensions and inflow velocity for the case of $AR = 5$ are chosen to match the parameters of the experiment in [15]. The nozzle exit velocity U_0 is 23 m/s, and the short side of the rectangle L_2 is 10 mm. The corresponding Reynolds number based on L_2 and U_0 is 14,470. The half-velocity widths are chosen in the transverse and spanwise directions as $y_{1/2}$ for normalization. Fig. 2 shows that the results from the Smagorinsky SGS model and the dynamic subgrid scale eddy viscosity model proposed by Germano et al. [16] both agree well with the experimental results. To save computational time, the Smagorinsky SGS model is selected.

To further consider grid dependence, three sets of calculations are carried out with different grid sizes. The numbers of grid points are $608 \times 130 \times 130$, $182 \times 66 \times 66$, and $92 \times 34 \times 34$, where the aspect ratio of the nozzle is kept at 2 for all three simulations. Streamwise velocity distributions, as shown in Fig. 3, indicate that the mean streamwise velocity decay does not vary significantly when the number of grid points is changed from $182 \times 66 \times 66$ to $608 \times 130 \times 130$. However, large variations exist between the simulation results for $182 \times 66 \times 66$ grid points and $92 \times 34 \times 34$ grid points.

Fig. 4 shows distributions of simulated rms velocities in the streamwise direction using different grids. In general, results of rms velocities obtained using a coarse grid of $92 \times 34 \times 34$ are higher than those obtained with finer grids of $182 \times 66 \times 66$ and $608 \times 130 \times 130$. This indicates that more energies are resolved within the subgrid when a coarse grid is used. However, results obtained by the two grids of $182 \times 66 \times 66$ and $608 \times 130 \times 130$ are similar. Although there are some differences between the two finer grids for simulations downstream of the nozzle, such differences are acceptable particularly as a long computational time is needed when the finest grid is used. For the rest of this paper, a moderate grid system of $182 \times 66 \times 66$ points is used.

3.2. Characteristics of the coherent structure of the methane non-premixed jet flame

During ignition of the rectangular methane non-premixed flame jet, a pair of vortices is present in the near field. Fig. 5 shows nephograms of the predicted temperature distributions and the shapes of the flame from 0.779 to 0.948 s. At 0.779 s, there is a pair of large vortices on either side of the flame at about $x = 5$. Between 0.792 s and 0.87 s, this pair of large vortices propagates downstream and a new pair of vortices is formed upstream of the former pair of large vortices. In general, when a pair of vortices reaches about $x = 20$, another pair is formed at about $x = 5$.

In this paper, assuming the start of the vortex cycle to be 0.779 s, detailed structures of two pairs of large vortices in the near field are given in Fig. 5 at 0.857, 0.87 and 0.883 s. Compared with the flame structures at 0.857 and 0.883 s, the flame structure at 0.87 s is very much similar to that at 0.779 s, particularly in terms of the bottom of the vortex pair near the nozzle of the rectangular jet. Thus, the period of vortex evolution is determined as 0.091 s.

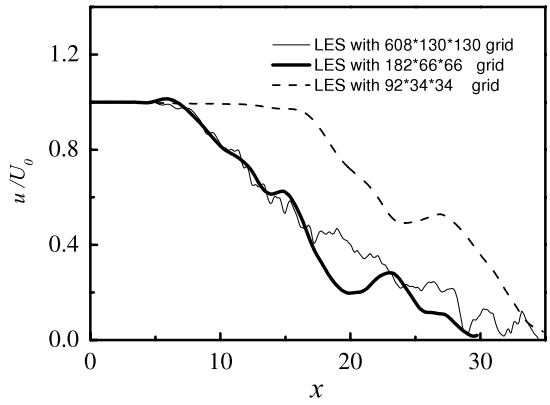

Fig. 3. Mean streamwise velocity along the centerline for $AR = 2$.

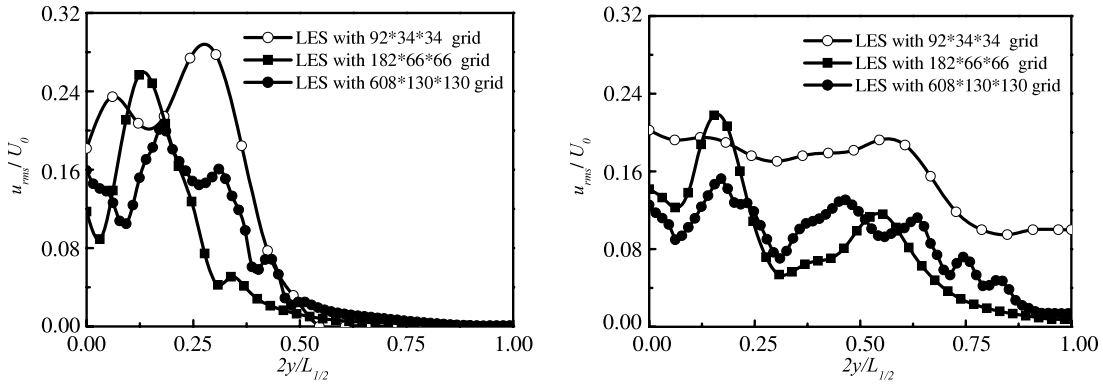

(a) At $x = 10$. (a) At $x = 20$.

Fig. 4. Distributions of simulated rms velocities using different grid sizes.

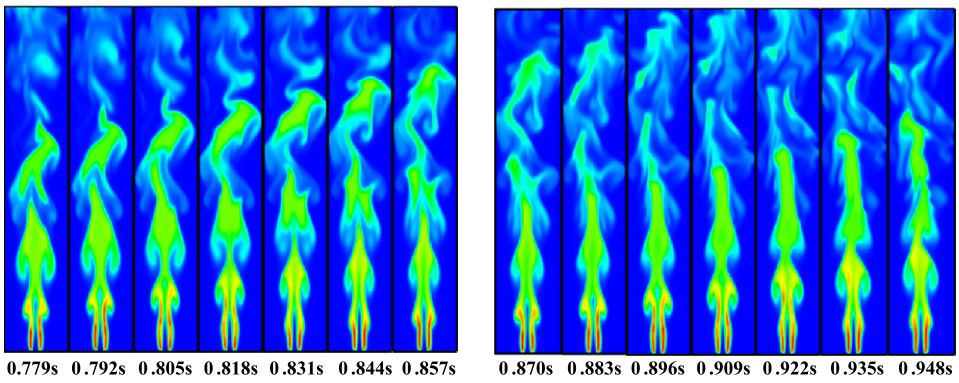

(a) First cycle. (b) Second cycle.

Fig. 5. Evolution of coherent structures of the methane flame.

3.3. The flame structure in the near field

Fig. 6 shows the structure of the rectangular methane jet in the near field. The flame shape has three distinct stages which are also observed in experiments, as shown in Fig. 7. In the initial stage, there is a thin and stable rectangular laminar reaction sheet attached to the nozzle. In the expansion stage, the reaction sheet becomes unstable due to upstream reaction and entrainment of the ambient air. The shape of the flame is dominated by the heating effect in this expansion stage. After that, due to rapid oxygen consumption caused by combustion and strong buoyancy, air entrainment becomes stronger. Thus, the first pair of large vortices exists downstream of the flow field, and is dominated by the entrainment of ambient air.

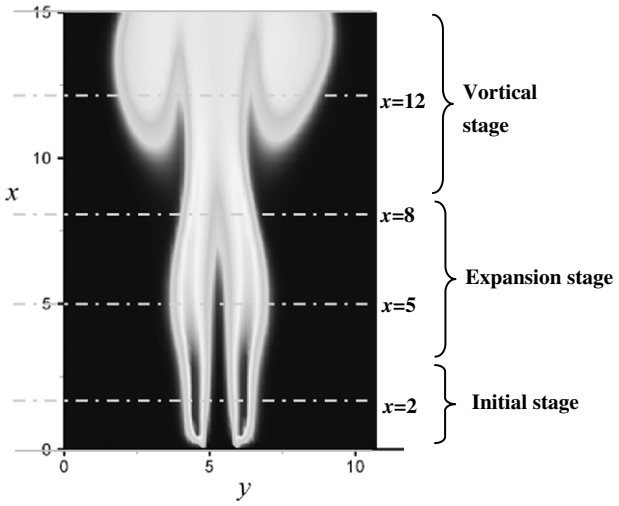

Fig. 6. Flame structure in the near field.

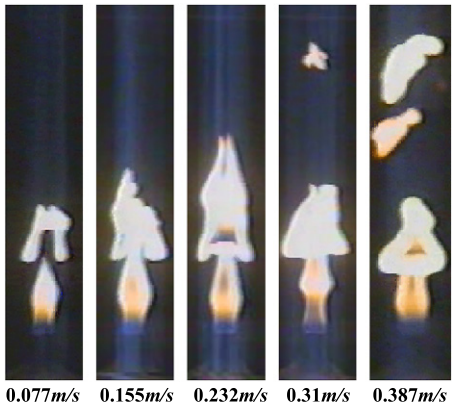

Fig. 7. Experimental results for the flames with different jet velocities.

As illustrated in Fig. 8, detailed species mass fraction distributions and reaction rates are given at four locations in the near field. The line at $x = 2$ is located in the initial stage, two lines at $x = 5$ and $x = 8$ are located in the expansion stage, and the line at $x = 12$ is located in the vortical stage. Fig. 8(a) shows one-dimensional distributions of species mass fractions and reaction rates of methane at $x = 2$; the distribution of the methane reaction rate indicates that combustion takes place at the thin interface between the methane jet and ambient air. Accordingly, the high mass fraction of H_2O is mainly at the interface where combustion takes place, and the distribution of the H_2O mass fraction is in the shape of a "saddle". In the initial stage, there is a large amount of unburned methane inside the flame, and the mass fraction of methane still has the value of 1.0 at the center of the flame and it quickly reduces to zero when it crosses the thin reaction region from inside of the flame. For the oxygen concentration, the mass fraction of oxygen also quickly reduces to zero when crossing the thin reaction region from outside of the flame; the distribution of the oxygen mass fraction is in the shape of a "basin", as found for most diffusion flames.

Fig. 8(b) and (c) show distributions of species mass fractions and reaction rates of methane at $x = 5$ and $x = 8$ in the expansion stage. A reaction zone exists at the thin interface between the methane jet and the ambient air. However, with the development of combustion and diffusion, methane concentration at the center is gradually reduced. In addition, the "saddle" of the H_2O concentration distribution becomes flat due to diffusion. Compared with the methane reaction rate at $x = 2$, the reaction rates at $x = 5$ and $x = 8$ are reduced.

During the initial expansion stages of the flame in the near field, both the species mass fraction and the reaction rate distributions are regular. Combustion takes place at the interface between the methane jet and the surrounding air. With the coherent structures developing, the interface between the fuel and air becomes more complex due to vortex movement. Fig. 8(d) shows distributions of species mass fractions and reaction rates of methane at $x = 12$. For the methane mass fraction distribution, there is a peak along the center of the flame, but its peak value reduces to about 0.15 due to consumption by combustion and diffusion by the vortices. For the oxygen mass fraction distribution, there are two peaks in the center due to entrainment of the surrounding air by the vortical movement. At $x = 12$, multi-reaction zones exist with low reaction rates

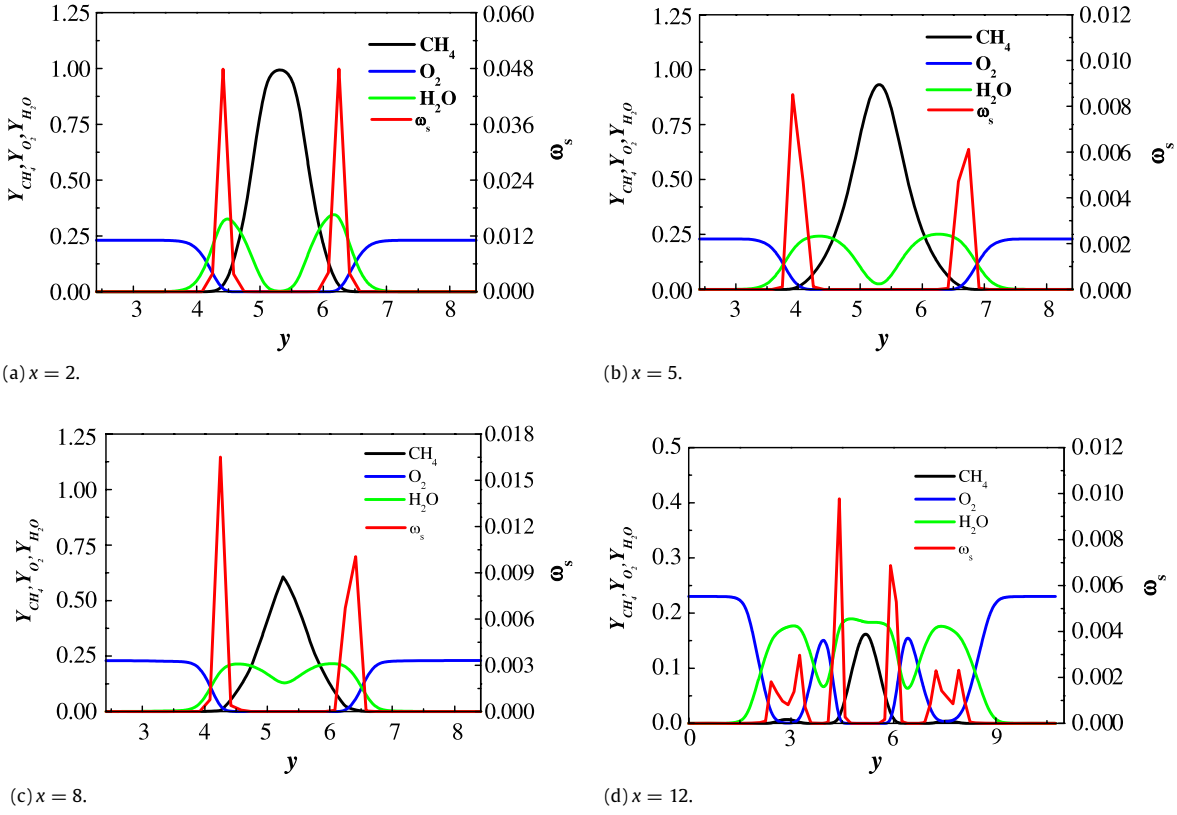

Fig. 8. One-dimensional species distribution.

occurring at the outer edge of the flame, and high reaction rates at the inner edge of the flame. Compared with the flame in the initial stage and the expansion stage, the flame becomes wider at $x = 12$ due to the vortex movement.

4. Conclusions

Characteristics of a rectangular methane non-premixed flame jet are investigated by large eddy simulation. The results show that there are a series of large scale vortices, i.e. coherent structures in the rectangular methane non-premixed flame, with the feature of quasi-periodic evolution for coherent structures. Simulated results for the periodic coherent structures agree well with experimental data for the rectangular methane non-premixed flame jet.

In the near field of the rectangular methane non-premixed flame jet, the shape of the flame can be classified into three typical stages, i.e. the initial stage, the expansion stage and the vortical stage. Downstream of the flame, strong streamwise vortices exist and ambient cold oxygen is drawn into the flame with the formation of black spots within the flame. When two pairs of strong spanwise and streamwise vortices coexist downstream of the flame, the stretch effect and the surrounding air entrainment caused by them lead to breaking up of the flame.

Acknowledgements

This work was partially supported by the Ministry of Science and Technology of China under the National Key Basic Research Special Funds (Grant No. 2001CB409600), the National Natural Science Foundation of China (Grant No. 50006006), and the AMSS-PolyU Joint Research Institute of The Hong Kong Polytechnic University (Project Account Code 1-BA05).

References

[1] S.C. Crow, F.H. Champagne, Orderly structure in jet turbulence, Journal of Fluid Mechanics 48 (3) (1971) 547–591.
[2] A.A. Sfeir, The velocity and temperature fields of rectangular jets, International Journal of Heat and Mass Transfer 19 (1976) 1289–1297.
[3] A. Krothapalli, D. Baganoff, K. Karamcheti, On the mixing of rectangular jet, Journal of Fluid Mechanics 107 (1981) 201–220.
[4] R.S. Miller, C.K. Madnia, P. Givi, Numerical simulation of non-circular jets, Computers and Fluids 24 (1) (1995) 1–25.
[5] F.F. Grinstein, K. Kalilasanath, Three-dimensional numerical simulations of unsteady reactive square jets, Combustion and Flame 100 (1–2) (1995) 2–10.
[6] F.F. Grinstein, C.R. DeVore, Dynamics of coherent structures and transition to turbulence in free square jets, Physics of Fluids 8 (5) (1996) 1237–1251.

[7] B. Rembold, N.A. Adams, L. Kleiser, Direct numerical simulation of a transitional rectangular jet, International Journal of Heat and Fluid Flow 23 (5) (2002) 547–553.
[8] J.E. Rehm, N.T. Clemens, The large-scale turbulent structure of nonpremixed planar jet flames, Combustion and Flame 116 (1999) 615–626.
[9] D.S. Louch, K.N.C. Bray, Vorticity and scalar transport in premixed turbulent combustion, Proceedings of the Combustion Institute 27 (1998) 801–810.
[10] A. Kempf, A. Sadiki, J. Janicka, Prediction of finite chemistry effects using large eddy simulation, Proceedings of the Combustion Institute 29 (2002) 1979–1985.
[11] A.X. Sengissen, A.V. Giauque, G.S. Staffelbach, M. Porta, W. Krebs, P. Kaufmann, T.J. Poinsot, Large eddy simulation of piloting effects on turbulent swirling flames, Proceedings of the Combustion Institute 31 (2007) 1729–1736.
[12] J. Smagorinsky, General circulation experiments with primitive equations—I, the basic experiment, Monthly Weather Review 91 (1963) 99–105.
[13] P. Jiang, Y.C. Guo, C.K. Chan, W.Y. Lin, Frequency characteristics of coherent structures and their excitations in small aspect-ratio rectangular jets using large eddy simulation, Computers and Fluids 36 (2007) 611–621.
[14] H.N. Najm, A conservative low mach number projection method for reacting flow modeling, in: Chan S (Ed.), Transport Phenomena in Combustion, vol. 2, Washington, DC, 1996, pp. 921–932.
[15] Y. Tsuchiya, C. Horikoshi, T. Sato, On the spread of rectangular jets, Experiments in Fluids 4 (1986) 197–204.
[16] M. Germano, U. Piomelli, P. Moin, W.H. Cabot, A dynamic subgrid-scale eddy viscosity model, Physics of Fluids A 3 (7) (1991) 1760–1765.